Electronic Supplementary Material (ESI) for Journal of Materials Chemistry A.

Supplementary Materials

$BiVO_4$ Optimized to Nano-Worm Morphology for Enhanced

Kajal Kumar Dey[†‖], Soniya Gahlawat[†], Pravin P. Ingole[†]*

[†] Department of Chemistry, Indian Institute of Technology Delhi, New Delhi 110016, India.

[‖]Rajendra Singh Institute of Physical Sciences for Studies and Research, V.B.S. Purvanchal University, Jaunpur 222003, India

* E-mail: ppingole@chemistry.iitd.ac.in, Phone: +91 11 2659 7547, Fax: +91 11 2658 1102.

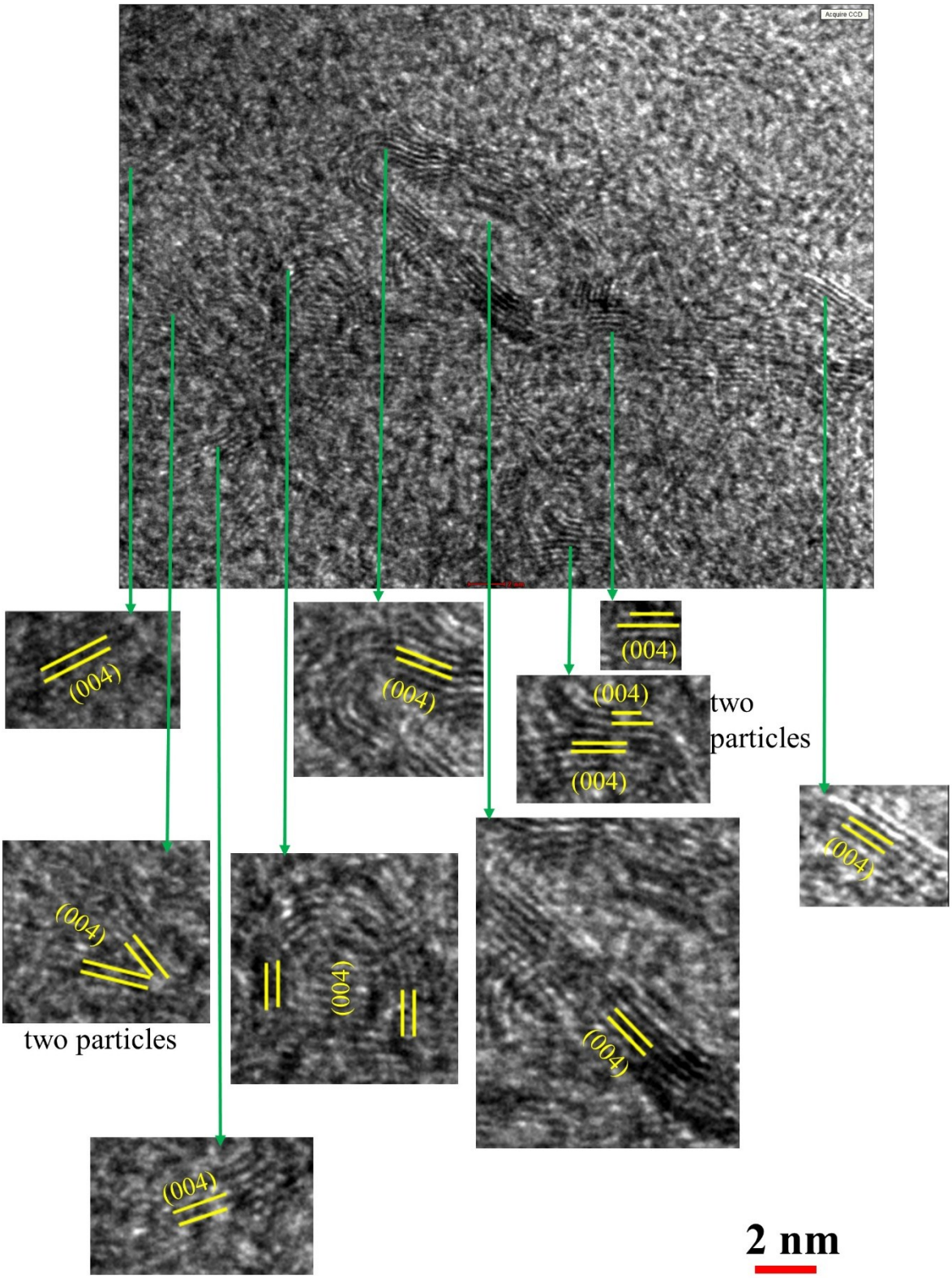

Figure S1 High resolution TEM micrograph displaying the presence of several nano-worm $BiVO_4$ particles. Lattice fringes of the individual particles have been provided below with magnified cropped portions of the main image.

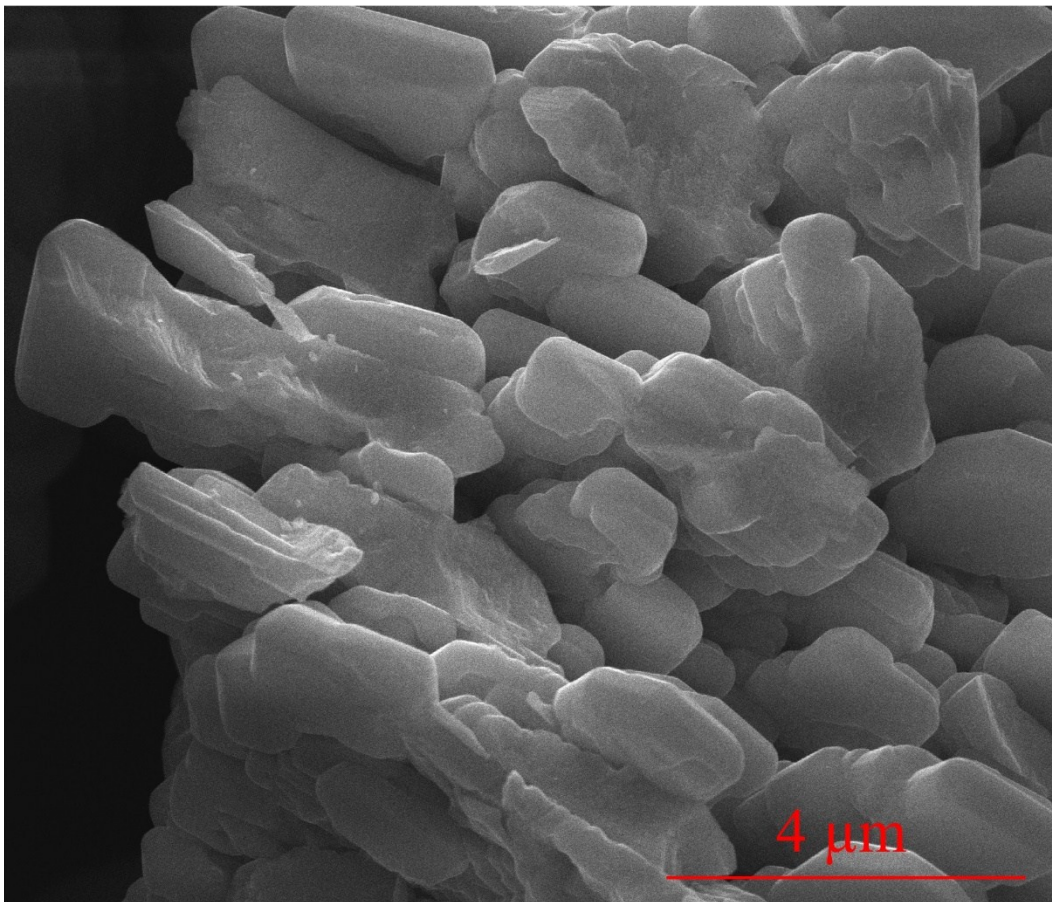

Figure S2 FESEM image of the bulk surface morphology of the $BiVO_4$ particles synthesized followed by 18 hours of hydrothermal treatment

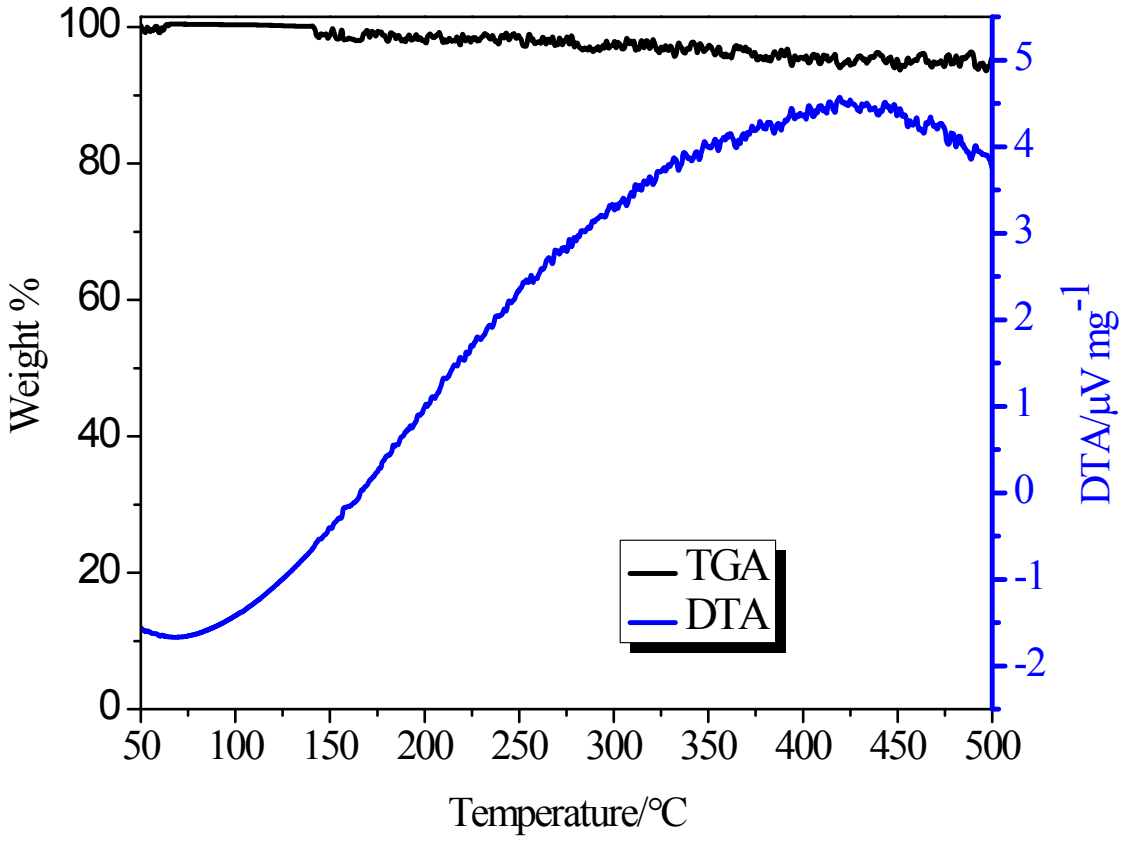

Figure S3 TGA and DTA curve of BV0 recorded within the temperature range of 50-500 ^{0}C

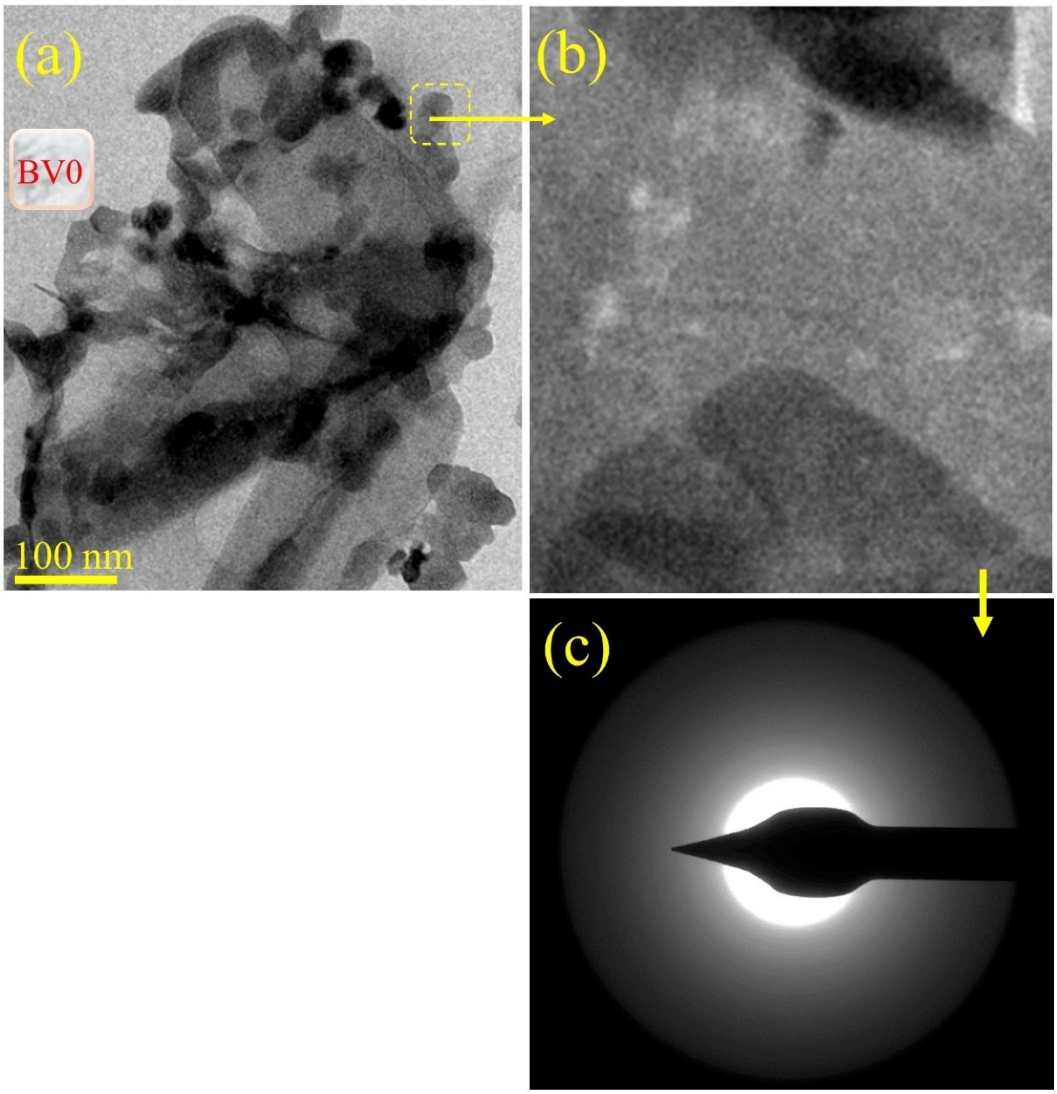

Figure S4 (a) TEM micrograph of BV0 showing the coexistence of sheet-like structures and particles, (b) a magnified portion of BV0 sheet and (c) the corresponding SAED pattern

Estimation of percentage of nano-worm particles in BVNW

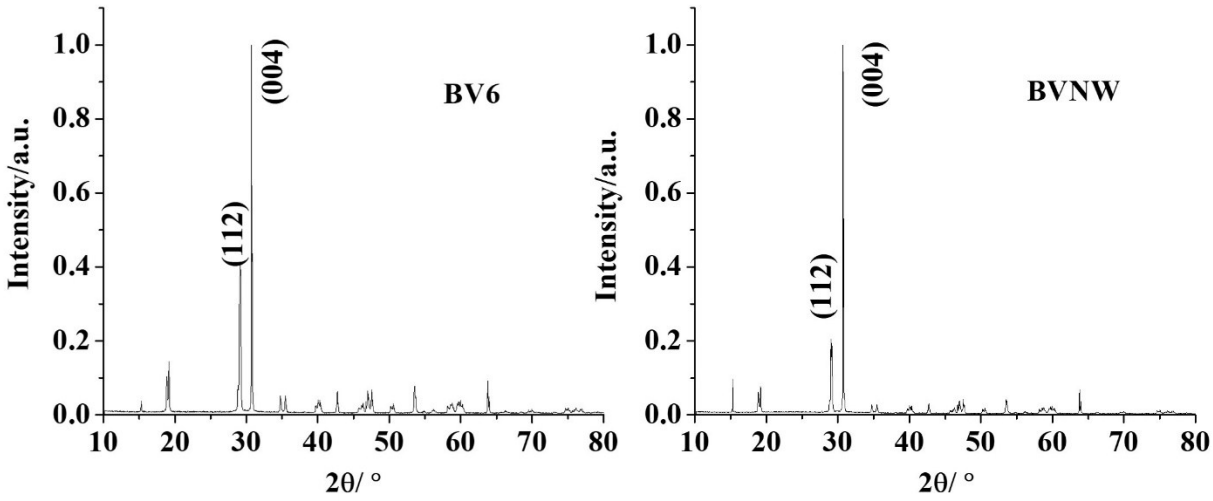

Figure S5 Normalized XRD patterns for BV6 and BVNW

In BV0, tetragonal scheelite particles of $BiVO_4$ are present. Following the hydrothermal treatment, tetragonal scheelite converts to monoclinic scheelite $BiVO_4$ with (004) planes being more intense. Upon 6 hours of hydrothermal treatment we get polycrystalline $BiVO_4$ materials (BV6) with dominant (004) peaks (Figure S5). BV6 contained both $BiVO_4$ sheets along with nanoparticles (Figure 3). From the normalized XRD pattern of BV6

$I_{(112)}/I_{(004)}$ = 1:0.42 [$I_{(hkl)}$ = intensity of the hkl peak)

The transformation, upon 18 hours of hydrothermal treatment, eventually leads to the disintegration of BV6 sheets and the formation of $BiVO_4$ nano-worms having single crystalline (004) nature (Figure 3). But the overall nature being polycrystalline, as observed from its XRD pattern (Figure S5), evidently polycrystalline $BiVO_4$ particles are simultaneously present in this sample.

From the normalized XRD pattern of BVNW

$I_{(004)}/I_{(112)}$ = 1:0.19

If the fraction of nano-worm particles in BVNW sample is 'x'; assuming the nano-worms contribute entirely to $I_{(004)}$ and the other polycrystalline particles in BVNW contributes to $I_{(004)}$ and $I_{(112)}$ in the same ratio as in BV6; we have

$$\frac{x \times 1 + (1-x) \times 1}{(1-x) \times 0.42} = \frac{1}{0.19}$$

or, x = 0.548 or ~55 %

So, roughly, 55% of $BiVO_4$ particles in BVNW are the nano-worms.

It should be mentioned that this estimation method is not entirely accurate as some of the approximations are pretty loose, e.g. ‘other polycrystalline particles in BVNW contributes to $I_{(004)}$ and $I_{(112)}$ in the same ratio as in BV6’, may not hold up entirely, as the morphology evolution and concomitant crystallographic transformation are dynamic process; so, that ratio will probably not be same. However, we can get a decent enough approximation using this method.

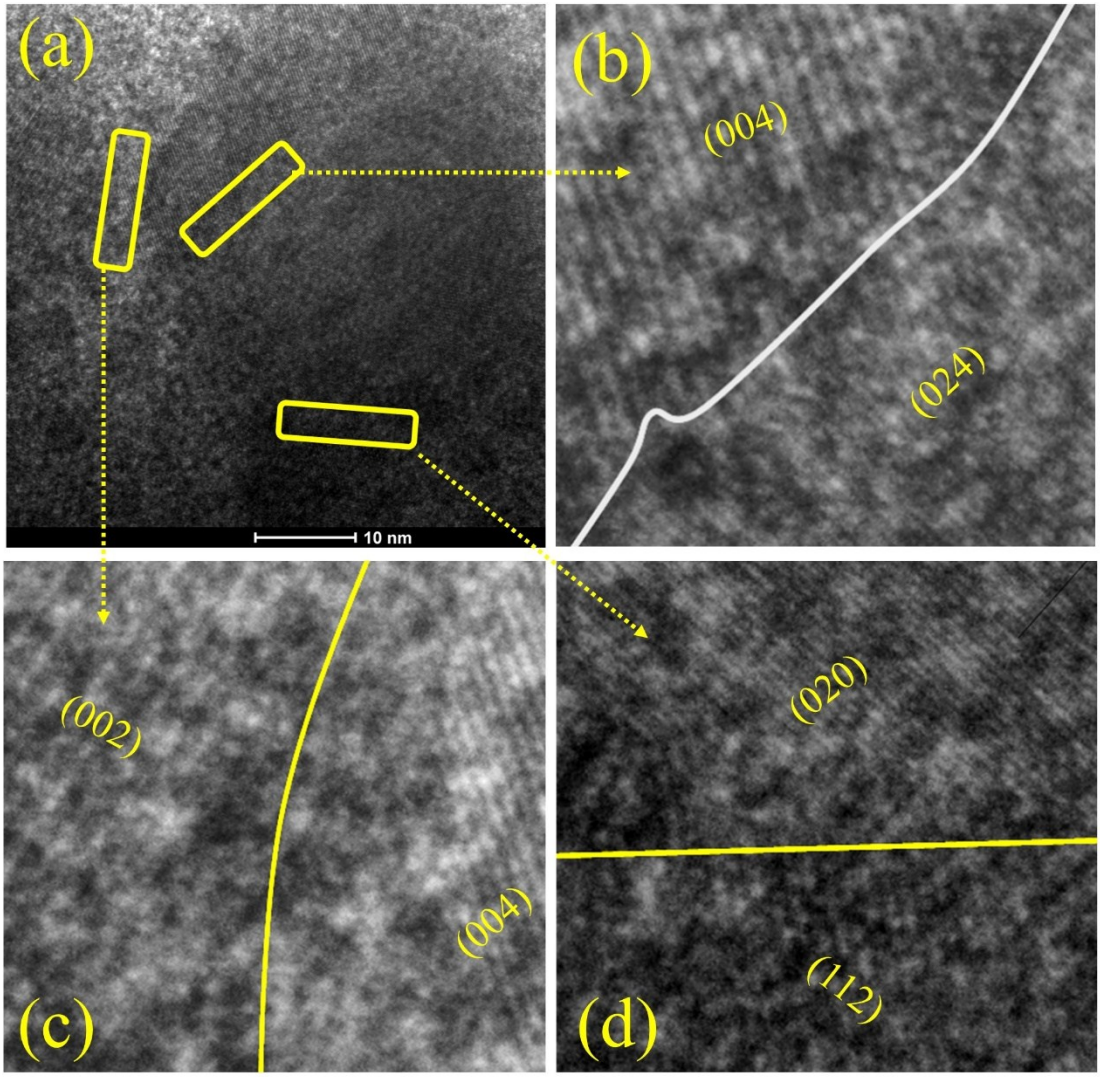

Figure S6 (a) HRTEM micrograph of BV6. The rectangular boxes represent the crystallographic defect areas; (b), (c) and (d) provides magnified version of those defects. The solid lines indicate the grain boundaries.

Figure S6 reveals crystallographic defect structures associated with BV6 nanoparticles observed through the TEM micrographs. It is well known that the presence of crystallographic lattice defects such as grain boundary can impede charge carrier transfer as such defects tend to act as potential barriers. These kinds of defects can be particularly pronounced during incomplete growth of particles undergoing constant changes in the form of dissolution, nucleation and growth. BV6 represents an initial phase during the hydrothermal treatment of Scheelite tetragonal $BiVO_4$ sheets evolving into the nano-worm like particles. Grain boundary usually is a feature of polycrystalline materials and indicates the interface between two crystallite regions where the (hkl) planes of both

terminate suddenly. In figure S6(a) we have selected three such regions enclosed by rectangular boxes that contain the grain boundary (GB) between different crystallite regions. Subsequent three figures i.e. S6 (b), (c) and (d), represents magnified versions of these defects where the GBs have been identified by solid lines. S6(b) represents the GB between (004) and (024) crystallite regions. S6(c) represents the GB between (002) and (004) crystallite regions and S6(d) represent the GB between (020) and (112) crystallite regions. There are numerous such regions but we chose to highlight three of them for the sake of simplicity. Presence of such a defect rich structure is a direct consequence of BV6 being an intermediate during the morphology transformation. It also underscores the presence of numerous potential barriers in the BV6 structure that inhibits the charge transfer and limiting the photoelectrochemical performance of this material.

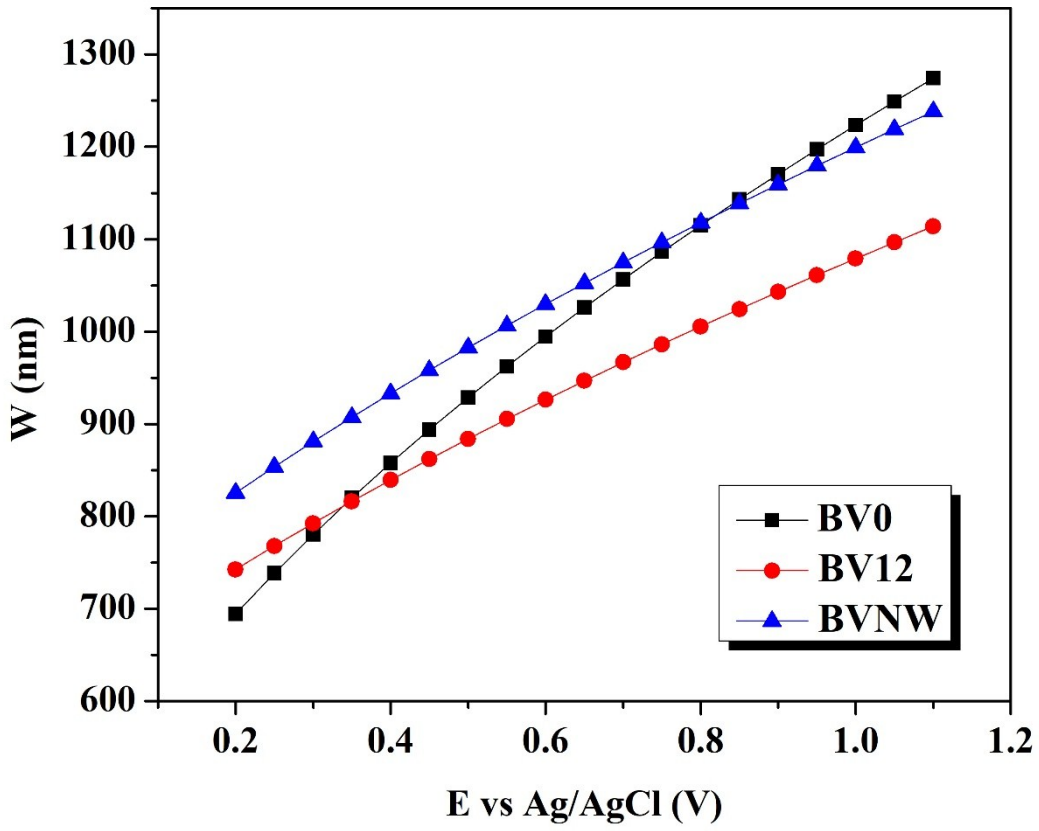

Figure S7 Plots of space charge layer width against the applied potential for the $BiVO_4$ samples

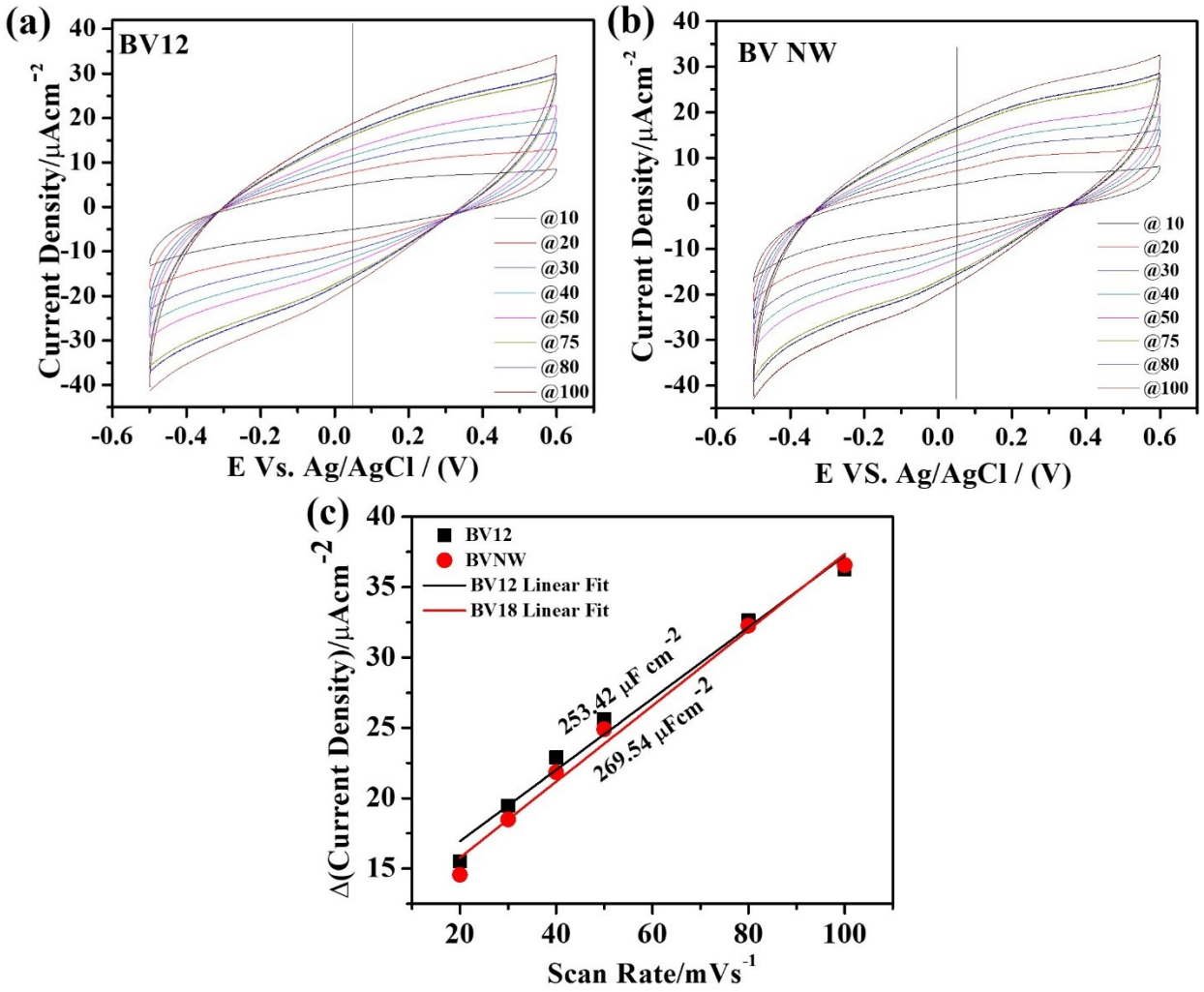

Figure S8 (a) and (b) CVs recorded for BVNW and BV12 at various scan rates in the phosphate buffer solution (pH 7.00). (c) linear fitting of Δ (current density) vs scan rates at 0.05 V vs Ag/AgCl.

Electrochemically active surface area (ECSA) of the samples were estimated via double layer capacitance method [1]using cyclic voltammetry (CVs) recorded in the non-Faradaic region (-0.5 V to 0.6 V vs Ag/AgCl). CVs were recorded at different scan rates e.g. 10, 20, 30, 40, 50, 75, 80 and 100 mV/s (Figure S7 (a) and (b)). The difference in current density (Δ (current density)) between the anodic and cathodic current at the potential of 0.05 V was calculated from the CV curves recorded at each of the scan rates. Δ (current density) was plotted against corresponding scan rates for both BV12 and BVNW (Figure S7 (c)) and half of the slope of the linear fitted plots is taken as the double layer capacitance (C_{dl}). The ECSA values are usually accepted as proportional to the corresponding C_{dl} values. Here, the obtained Cdl values for BV12 and BVNW electrodes are 253.42 μF cm^{-2} and 269.54 μF cm^{-2}.

Calculation of Charge transport efficiency (η_{trans})

Chopped LSV measurement was carried out in Phosphate buffer solution (PBS; pH 7.00). The corresponding photocurrent is expressed as J_{H_2O}.

PEC measurement with hole scavenger was recorded in PBS solution with the addition of 0.5 (M) sodium sulfite. The pH was adjusted to 7.00 and the corresponding photocurrent is expressed as $J_{Na_2SO_3}$.

Charge transport efficiency (η_{trans}) is calculated as $\eta_{trans} = J_{H_{2O}} / J_{Na_2SO_3}$

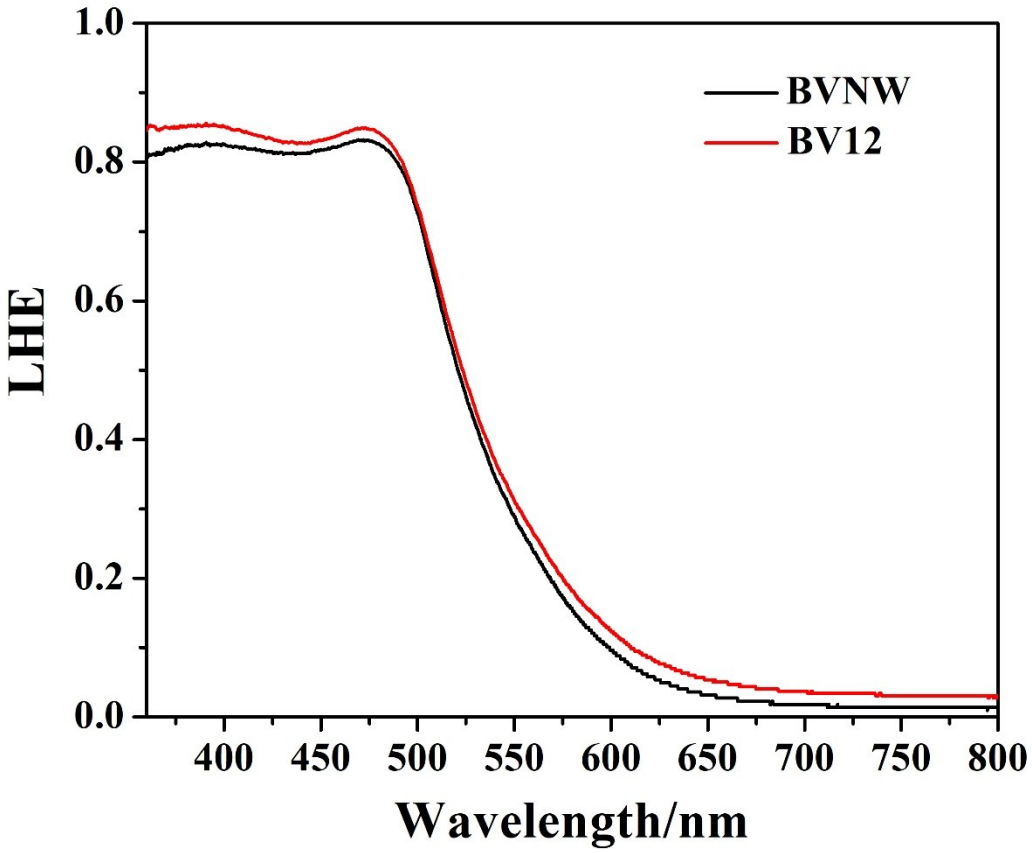

Figure S9. Light harvesting efficiency of the photoanodes

Light harvesting efficiency (LHE) of the photoanodes was calculated by following the equation:

$LHE = 1 - 10^{-A(\lambda)}$

Where, A = absorbance at wavelength λ.

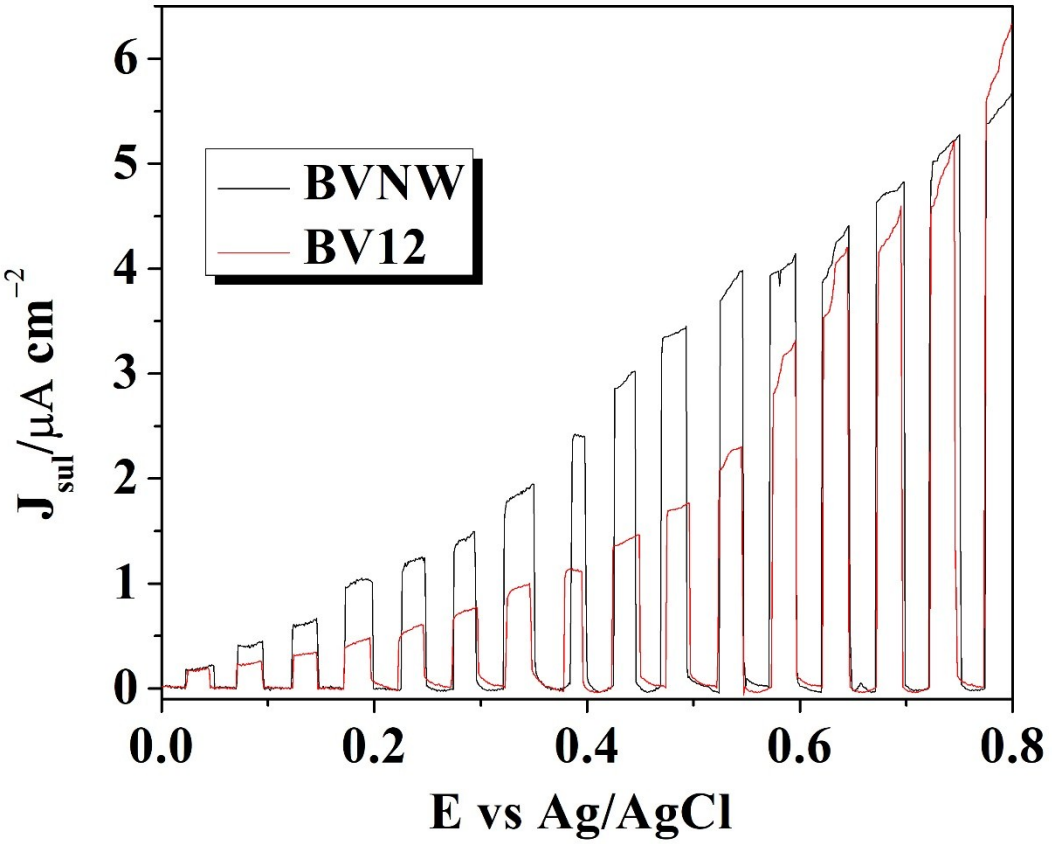

Figure S10. Chopped J-V curves for BVNW and BV12 recorded in phosphate buffer solution in presence of 0.5 (M) Na_2SO_3.

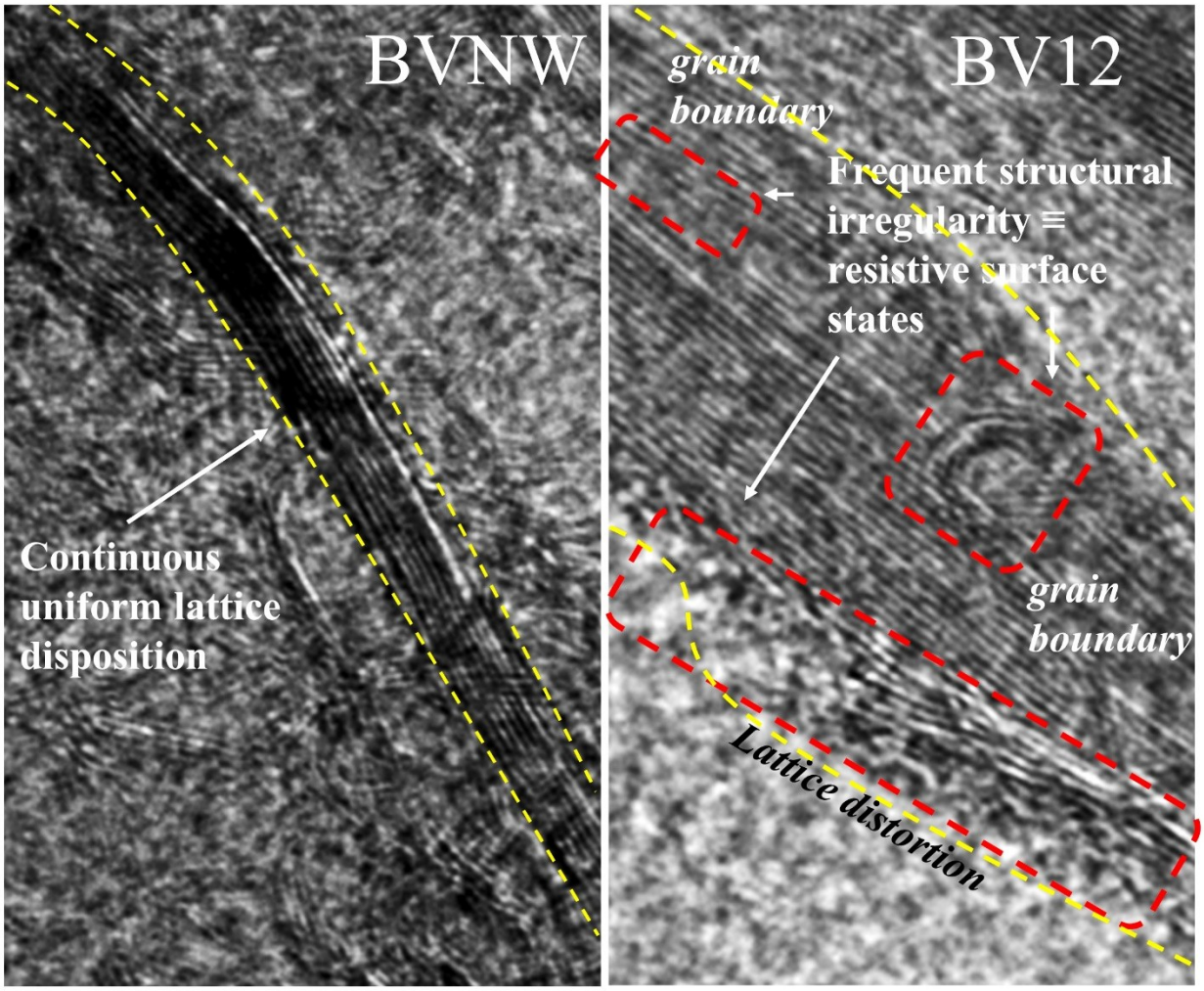

Figure S11. Left side-high resolution TEM micrograph of a fully grown $BiVO_4$ nanoworm (BVNW). Right side- significant portion of a relatively wide BV12 rod. Individual particles are bound by dashed yellow lines.

Parameters / Sample	R_S/Ω	$(R_{CT}/\Omega)/10^5$	Q (CPE)	
			$(Y_0/F)/10^{-5}$	n
BV0	14.13	2.959	2.569	0.96
BV6	16.39	3.933	2.78	0.95
BV12	13.78	2.289	2.736	0.94
BVNW	15.08	1.091	3.294	0.95

Table S1 Tabular representations of the electrical components obtained from fitting the experimental EIS data in an appropriate circuit model

Supplementary References

1 K. K. Dey, S. Jha, A. Kumar, G. Gupta, A. K. Srivastava and P. P. Ingole, *Electrochim. Acta*, 2019, **312**, 89–99.